A force-balanced control volume finite element method for multi-phase porous media flow modelling

J. L. M. A. Gomes[1,3], D. Pavlidis[1,2,*,†], P. Salinas[1,2], Z. Xie[1,2], J. R. Percival[2], Y. Melnikova[1,2], C. C. Pain[1,2] and M. D. Jackson[1]

[1]*Novel Reservoir Modelling and Simulation Group, Department of Earth Science and Engineering, Imperial College London, London, UK*
[2]*Applied Modelling and Computation Group, Department of Earth Science and Engineering, Imperial College London, London, UK*
[3]*Environmental and Industrial Fluid Mechanics Group, School of Engineering, University of Aberdeen, Aberdeen, UK*

SUMMARY

A novel method for simulating multi-phase flow in porous media is presented. The approach is based on a control volume finite element mixed formulation and new force-balanced finite element pairs. The novelty of the method lies in (i) permitting both continuous and discontinuous description of pressure and saturation between elements; (ii) the use of arbitrarily high-order polynomial representation for pressure and velocity and (iii) the use of high-order flux-limited methods in space and time to avoid introducing non-physical oscillations while achieving high-order accuracy where and when possible. The model is initially validated for two-phase flow. Results are in good agreement with analytically obtained solutions and experimental results. The potential of this method is demonstrated by simulating flow in a realistic geometry composed of highly permeable meandering channels. © 2016 The Authors International Journal for Numerical Methods in Fluids Published by John Wiley & Sons Ltd

1. INTRODUCTION

Numerical modelling of multi-phase flows in porous media has applications in a wide range of disciplines, including hydrocarbon and groundwater production, safety assessment of deep geological disposal of radioactive waste, and carbon capture and storage [1–4]. Such applications often include complex geometries with irregular (and often internal) boundaries between rock types with contrasting porosity and permeability. Accurately capturing these complex geometries is a key challenge when simulating such flows.

Finite difference methods have been extensively used for modelling fluid flows in porous media [5–7]. However, they are strongly dependent on mesh quality and orientation, and cannot easily represent complex geometries. In addition, finite difference methods can produce excessive numerical dispersion in heterogeneous porous media flows [8].

The geometrical flexibility of finite element methods (FEM) has been shown to overcome these deficiencies. Among FEM-based formulations for porous media, the control volume (CV) FEM

(CVFEM) is increasingly popular as it can guarantee local mass conservation, it has the potential to be high-order accurate and is able to use tetrahedral, geometry-conforming elements [9–12]. Huber and Helmig [13] demonstrated that the vertex-centred, finite volume FEM (or box scheme) can achieve similar goals (see also [14]).

Durlofsky [15, 16] compared the performance of a mixed FEM formulation (piecewise linear in velocity and piecewise constant in pressure) and the classical CVFEM for single phase Darcy flows. It was concluded that the latter is computationally more efficient and numerically more accurate than the former for problems involving a (relatively) small number of degrees of freedom. Moreover, for complex heterogeneous problems with sharp changes in material properties, the mixed FEM formulation often led to physically unrealistic solutions. Cumming *et al*. [17] demonstrated that a CVFEM-based discretisation could be used to solve the Richards equation (coupled mass conservation and Darcy equations) in heterogeneous porous media with relatively small computational overhead, compared with traditional, coupled velocity pressure-based formulations. Mass balance was enforced as described by Kirkland *et al*. [18] (see also [9, 19]). However, CVFEM often requires high-resolution meshes in regions where material properties vary abruptly, such as permeability contrasts at (for example) fracture-matrix interfaces, or boundaries between different rock types. CV boundaries span FEs where material properties are defined; therefore, some average value of the permeability must be calculated across CV interfaces. This often leads to excessive numerical dispersion, especially in highly heterogeneous media [20, 21].

Discontinuity-capturing schemes (e.g. shock waves, contact surface or material discontinuities [22, 23]), were originally developed to resolve sharp changes in solution fields such as velocity or saturation. Related discontinuity-capturing schemes include the discontinuous Galerkin FEM (DGFEM) scheme in which continuity of the solution is not explicitly enforced, allowing sharp changes in the solution fields to be captured. The DGFEM scheme is stabilised, locally conservative and designed to achieve high-order accuracy. DGFEM solution fields are allowed to be discontinuous at the element faces; thus, the solution is able to handle discontinuities in material properties at internal boundaries. In addition, DGFEM is well suited to deal with interface problems by incorporating specially designed interface fluxes. These properties have attracted the attention of the porous media flow community over the past 15 years (see [24–26]) and are utilised here.

In this paper, a novel CVFEM formulation, which is conservative and consistent is presented. The continuity equations are embedded into the pressure equation to enforce mass conservation and the exact force balance. The P_nDG-$P_m[DG]$ family of triangular and tetrahedral FE pairs is used to discretise velocity and pressure in space. For this element type, the velocity field is represented by nth-order polynomials that are discontinuous across elements, while the pressure field is represented by mth-order polynomials that may be continuous (termed P_nDG-P_m) or discontinuous (termed P_nDG-P_mDG) across elements. CVs are dual to the pressure mesh. The formulation employs an implicit algorithm with respect to time that is less restrictive than the implicit pressure–explicit saturation (IMPES) scheme often adopted in porous media flow problems (e.g. [5, 11]).

The method is demonstrated using two families of element pairs: the P_nDG-P_m pair which can allow the velocity to exactly represent the pressure gradients in the flow solution for homogeneous material properties; and the $P_{n+1}DG$-P_nDG pair, which has similar properties to the P_nDG-P_{n+1} element pair, but allows a representation in which pressure, saturation and other solution variables are discontinuous across FE boundaries. This solves the long-standing problem described earlier with respect to the use of traditional CVFEM to capture sharp changes in material properties.

Results using this method in simple geometries have been previously reported in the literature (e.g. [27, 28]). However, the method has not been described in detail or thoroughly validated, and its potential has not been explored. The remainder of this paper is organised as follows. The governing equations and numerical methods employed to solve them are introduced in Section 2. Model set-up and results including comparison against reference data are given in Sections 3 and 4, respectively. Finally, concluding remarks are presented in Section 5.

2. GOVERNING EQUATIONS AND NUMERICAL FORMULATION

2.1. A novel representation of multi-phase Darcy flows

Darcy's law for immiscible multi-phase flow may be written in the form

$$\mathbf{q}_\alpha = -\frac{\mathcal{K}_{r_\alpha}\mathbf{K}}{\mu_\alpha}\left(\nabla p_\alpha - \mathbf{s}_{u\alpha}\right), \tag{1}$$

where $\mathbf{q}_\alpha$ is the α-th phase Darcy velocity, $\mathbf{K}$ is the absolute permeability tensor of the porous medium, $\mathcal{K}_{r_\alpha}(S_\alpha)$ is the phase relative permeability, which is a function of the phase saturation $S_\alpha(\mathbf{r},t)$. μ_α, p_α, ρ_α and $\mathbf{s}_{u\alpha}$ are the phase dynamic viscosity, pressure, density and source term, which may include gravity and/or capillarity, respectively.

Introducing a saturation-weighted Darcy velocity defined as $\mathbf{u}_\alpha = \mathbf{q}_\alpha/S_\alpha$, then Equation (1) may be rewritten as

$$\mathbf{v}_\alpha = \underline{\underline{\sigma}}_\alpha \mathbf{u}_\alpha = -\nabla p_\alpha + \mathbf{s}_{u\alpha}, \tag{2}$$

where $\underline{\underline{\sigma}}_\alpha = \mu_\alpha S_\alpha\left(\mathcal{K}_{r_\alpha}\mathbf{K}\right)^{-1}$ represents the implicit linearisation of the viscous frictional forces. The force per unit volume $\mathbf{v}_\alpha$, defined as $\underline{\underline{\sigma}}_\alpha\mathbf{u}_\alpha$, is used as a prognostic variable in this approach, as explained in Section 2.3.

In order to discretise Equation (2), a FE representation for $\mathbf{v}_\alpha$ and p is assumed, expressed in terms of their FE basis functions Q_j and P_j, respectively, as

$$\mathbf{v}_\alpha(\mathbf{r},t) = \sum_{j=1}^{\mathcal{N}_u} Q_j(\mathbf{r})\mathbf{v}_{\alpha,j}(t) \quad \text{and} \quad p(\mathbf{r},t) = \sum_{j=1}^{\mathcal{N}_p} P_j(\mathbf{r})p_j(t). \tag{3}$$

Here, $\mathcal{N}_u$ and $\mathcal{N}_p$ are the total number of degrees of freedom for the FE force and pressure representations. Each component of the weak form of the force balance (Equation (2)) is tested with the $\mathbf{v}_\alpha$ basis function space to obtain

$$\sum_E \int_{\Omega_E} Q_i\left(\mathbf{v}_\alpha + \nabla p - \mathbf{s}_{u\alpha}\right)dV + \oint_{\Gamma_E} Q_i\mathbf{n}\left(p - \tilde{p}\right)d\Gamma + \oint_{\Gamma_\Omega} Q_i\mathbf{n}\left(p - p_{\text{bc}}\right)d\Gamma = \mathbf{0}, \tag{4}$$

where Ω_E and Γ_E are the volume and boundary of element E, respectively, and Γ_Ω is the boundary of the computational domain. The numerical pressure $\tilde{p}$ appearing in the jump condition (second term in Equation (4)) is the arithmetic mean of the potentially discontinuous pressure across the element E. This term vanishes when a continuous formulation is used to discretise the pressure field. The last term in Equation (4) is used to weakly enforce the pressure level to p_{bc} on a computational domain boundary.

In matrix form, Equation (4) is

$$\mathbf{M}\underline{\mathbf{v}} = -\mathbf{C}\underline{\mathbf{p}} + \underline{\mathbf{s}}_u, \tag{5}$$

where $\underline{\mathbf{v}}$ and $\underline{\mathbf{p}}$ solution vectors are defined as

$$\underline{\mathbf{v}} = \left(\left(v_x, v_y, v_z\right)_{1,1}, \left(v_x, v_y, v_z\right)_{2,1}, \ldots, \left(v_x, v_y, v_z\right)_{\mathcal{N}_\alpha,\mathcal{N}_u}\right)^{\mathrm{T}} \text{ and}$$

$$\underline{\mathbf{p}} = \left(p_1, p_2, p_3, \ldots, p_{\mathcal{N}_p}\right)^{\mathrm{T}}.$$

$\mathcal{N}_\alpha$ is the number of phases, and v_x, v_y and v_z are the components associated with the x, y and z dimensions, respectively. Finally, the mass matrix $\mathbf{M}$, gradient matrix $\mathbf{C}$ and source vector $\underline{\mathbf{s}}_u$ are defined as

(a) P_1DG-P_2 (b) P_2DG-P_1DG
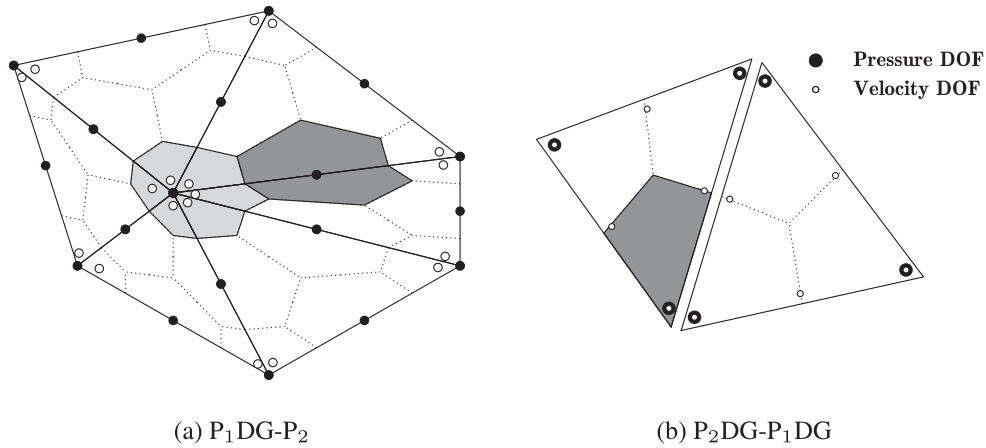
Figure 1. Two-dimensional (2D) representation of the element pairs presented in this work. Shaded areas denote CVs (in which saturation is stored), black points represent the pressure nodes, and white points the velocity nodes. Note that in (b) velocity and pressure nodes overlap in the triangles' vertices.

$$\left[\mathbf{M}^{(i,j)}\right]_{k,l} = \int_\Omega Q_k \left[\underline{\underline{\sigma}}_\alpha\right]_{i,j} Q_l \, dV,$$

$$\left[\mathbf{C}^{(i,i)}\right]_{k,l} = \int_\Omega Q_k \frac{\partial P_l}{\partial r_i} dV - \oint_{\Gamma_E} \frac{1}{2} Q_k n_i^{(E,l)} P_l \, d\Gamma - \oint_{\Gamma_\Omega} Q_k n_i P_l \, d\Gamma,$$

$$\left[\mathbf{s}_u^{(i,i)}\right]_k = \int_\Omega Q_k \left[\mathbf{s}_{u_\alpha}\right]_i dV - \oint_{\Gamma_\Omega} Q_k n_i p_{\text{bc}} \, d\Gamma,$$

where i and j are dimensions and k and l are the degrees of freedom of element E. Here, $\boldsymbol{n} = (n_1, n_2, n_3)^\mathrm{T}$ is the outward-pointing normal vector of the domain Ω. $\boldsymbol{n}^{(E,l)}$ is the normal to the boundary of element E and is outward-pointing if P_l takes support on E, and inward-pointing otherwise.

The saturations are computed in CV space, whereas the permeability tensor ($\mathbf{K}$) is assumed piecewise constant in FE space. Thus, the viscous-friction damping tensor $\underline{\underline{\sigma}}_\alpha$ is piecewise constant within the sub-CVs defined through intersections between the elements and CVs (Figure 1).

2.2. Control volume finite element types

In the formulation presented here, pressure, velocity, permeability and porosity are represented FE-wise; however, saturation, relative permeability and fluid properties such as viscosity and density are represented CV-wise. Figure 1 displays the two families of element types presented in this paper: Figure 1(a) shows the P_nDG-P_{n+1} element type, with $n = 1$, in two dimensions (2D). Here, the velocity field is linear and discontinuous (between elements) while pressure has a quadratic and continuous (between elements) representation with the CV's span various elements. Figure 1(b) shows the $P_{n+1}DG$-P_nDG element type, with $n = 1$ (also in 2D). Here, the velocity field is quadratic and discontinuous (between elements) whereas pressure has a linear and discontinuous (between elements) representation and the CV's do not span elements.

2.3. Finite element representation of velocity

From Equation (1), it can be seen that the velocity field depends, among other fields, on the absolute permeability, which is FE-wise, and the relative permeability, which is CV-wise. This means that the velocity representation is different in each CV. However, the quantity $\mathbf{v}_\alpha$ is homogeneous within an element, and this is stored using FE representation. To obtain the velocity $\mathbf{u}_\alpha$ in a particular CV within a FE, Equation (2) is used.

2.4. Saturation and global mass conservative equations

Here, the saturation conservation equations are discretised and the global mass balance equation is derived. In this work, fluids are assumed incompressible. The saturation equation can be written as

$$\phi \frac{\partial S_\alpha}{\partial t} + \nabla \cdot (\mathbf{u}_\alpha S_\alpha) = s_{cty,\alpha}, \tag{6}$$

where ϕ is the porosity and s_{cty} is a source term. Equation (6) is discretised in space by testing with CV basis functions M_i and with the θ-method in time

$$\int_\Omega M_i \frac{\phi \left(S_{\alpha i}^{n+1} - S_{\alpha i}^n\right)}{\Delta t} dV + \oint_{\Gamma_{CV_i}} \left[\theta^{n+\frac{1}{2}} \mathbf{n} \cdot \mathbf{u}_\alpha^{n+1} S_\alpha^{n+1} + \left(1 - \theta^{n+\frac{1}{2}}\right) \mathbf{n} \cdot \mathbf{u}_\alpha^n S_\alpha^n\right] d\Gamma$$
$$= \int_\Omega M_i s_{cty,\alpha}^{n+\theta} dV, \tag{7}$$

where $\mathbf{n}$ is the outward-pointing unit normal vector to the surface (Γ_{CV_i}) of the CV i and n is the current time level. More details on the numerical methods used to solve Equation (7) can be found in [29].

The global continuity equation is obtained by summing Equation (7) over all phases

$$\sum_{\alpha=1}^{\mathcal{N}_\alpha} \left\{ \int_\Omega M_i \frac{\phi \left(S_{\alpha i}^{n+1} - S_{\alpha i}^n\right)}{\Delta t} dV + \oint_{\Gamma_{CV i}} \left[\theta^{n+\frac{1}{2}} \mathbf{n} \cdot \mathbf{u}_\alpha^{n+1} S_\alpha^{n+1} + \left(1 - \theta^{n+\frac{1}{2}}\right) \mathbf{n} \cdot \mathbf{u}_\alpha^n S_\alpha^n\right] d\Gamma \right.$$
$$\left. - \int_\Omega M_i s_{cty,\alpha}^{n+\theta} dV \right\} = 0. \tag{8}$$

Equation (8) is also bounded by the constraint

$$\sum_{\alpha=1}^{\mathcal{N}_\alpha} S_{\alpha i}^n = 1, \quad \forall n. \tag{9}$$

Solving for $\mathbf{u}^{n+1}$ in matrix form, Equation (8) becomes

$$\mathbf{B}^T \underline{v}^{n+1} = \underline{s}_p. \tag{10}$$

Matrix $\mathbf{B}^T$ and vector $\underline{s}_p$ are not explicitly given because they are extremely lengthy in definition and detract from the clarity of the explanation.

2.5. Velocity at control volume interfaces

The velocity to be used at the interface between CV's in the saturation conservation (Equation (7)) and global continuity (Equation (8)) equations needs to be determined. On the CV faces, there is no information about the flow direction as the velocity is discontinuous at the CV boundaries. The discontinuities occur between (i) CVs within each FE and (ii) between elements when using the $P_{n+1}DG$-$P_n DG$ element pair.

In order to calculate the velocity across CV's within a FE, an average velocity at the interface of CVs i and j is defined as

$$\tilde{\mathbf{u}}_\alpha = \frac{1}{2} \left[\mathbf{u}_{\alpha_i} + \mathbf{u}_{\alpha_j}\right]. \tag{11}$$

From this, the interface velocities at either side of the interface can be obtained from

$$\tilde{\mathbf{u}}_{\alpha k} = \underline{\underline{\sigma}}_{\alpha k}^{-1} \tilde{\mathbf{v}}_\alpha, \quad k = \{i, j\}. \tag{12}$$

These velocities have the same direction and differ only in magnitude, so using them to define an upwind direction is not ambiguous. If an upwind method for calculating the interface velocity is applied then,

$$\tilde{\mathbf{u}}_\alpha = \tilde{\mathbf{u}}_{\alpha k}, \tag{13}$$

where $k = i$ if $\mathbf{n} \cdot \mathbf{u}_\alpha > 0$ (CV i outgoing information), and $k = j$ if $\mathbf{n} \cdot \mathbf{u}_\alpha < 0$ (CVi incoming information).

However, upwind methods yield dissipative solutions; therefore, in order to obtain a high-order approximation of the velocity at the interface, the saturation at the interface $\tilde{S}_\alpha$ is calculated using a FE representation of the saturation following the upwind direction. $\tilde{\underline{\underline{\sigma}}}_\alpha$ can then be calculated using second-order Taylor series

$$\tilde{\underline{\underline{\sigma}}}_\alpha = \underline{\underline{\sigma}}_{\alpha k} + \left(\tilde{S}_\alpha - S_{\alpha k}\right)\left(\frac{\partial \underline{\underline{\sigma}}_\alpha}{\partial S_\alpha}\right)_k + \frac{1}{2}\left(\tilde{S}_\alpha - S_{\alpha k}\right)^2\left[\frac{\left(\frac{\partial \underline{\underline{\sigma}}_\alpha}{\partial S_\alpha}\right)_k - \left(\frac{\partial \underline{\underline{\sigma}}_\alpha}{\partial S_\alpha}\right)_l}{(S_{\alpha k} - S_{\alpha l})}\right], \tag{14}$$

where $k = i$ and $l = j$, if $\mathbf{n} \cdot \mathbf{u}_\alpha > 0$ and, $k = j$ and $l = i$, if $\mathbf{n} \cdot \mathbf{u}_\alpha < 0$. Therefore, the final interface velocity (Equation (13)) can be obtained from

$$\tilde{\mathbf{u}}_\alpha = \tilde{\underline{\underline{\sigma}}}_\alpha^{-1}\left[\frac{1}{2}\left(\mathbf{v}_{\alpha i} + \mathbf{v}_{\alpha j}\right)\right], \tag{15}$$

The interface velocity obtained from Equation (15) is bounded to ensure that its normal component $\tilde{\mathbf{u}}_\alpha \cdot \mathbf{n}$ lies between $\tilde{\mathbf{u}}_{\alpha i} \cdot \mathbf{n}$ and $\tilde{\mathbf{u}}_{\alpha j} \cdot \mathbf{n}$. The result of this is also bounded between the velocities $\mathbf{v}_{\alpha i} \cdot \mathbf{n}$ and $\mathbf{v}_{\alpha j} \cdot \mathbf{n}$.

In a fully discontinuous formulation with $P_{n+1}DG\text{-}P_nDG$ element pairs, the interface velocity (now between neighbour elements) can not be calculated using Equation (15) due the elliptic nature of the discretised non-symmetric pressure equation, Equation (5). This means that information is propagated in all directions across the (discontinuous) domain, and hence, taking the upwind velocity as commonly performed within an element is not an adequate strategy.

For two neighbouring CV's i and j with common FE interface (e.g. Figure 1(b) for $P_2DG\text{-}P_1DG$ element pair), $\tilde{\mathbf{u}}_\alpha$ can be calculated by using a volume-weighted harmonic mean. However, the volume $\mathcal{V}$ of the CV and $\underline{\underline{\sigma}}_\alpha$ act on the velocity in a very similar way. Hence, the velocity at the interface is expressed as

$$\tilde{\mathbf{u}}_\alpha = \left(\mathcal{V}_j\underline{\underline{\sigma}}_{\alpha j}\mathbf{u}_{\alpha i} + \mathcal{V}_i\underline{\underline{\sigma}}_{\alpha i}\mathbf{u}_{\alpha j}\right)\left(\mathcal{V}_i\underline{\underline{\sigma}}_{\alpha i} + \mathcal{V}_j\underline{\underline{\sigma}}_{\alpha j}\right)^{-1}. \tag{16}$$

2.6. Weak enforcement of boundary conditions

Suitable boundary conditions for velocity can be applied by the discontinuous formulation earlier as well as by the upwinding in the continuous formulation. In fact, exactly the same boundary condition implementations, as used in the discontinuous formulation, can be applied across the boundaries of the domain by taking information from 'just outside' the domain rather than from the neighbouring elements.

Saturation boundary conditions are relatively straightforward. One typically takes the saturation from 'just outside' the domain ($S_{\alpha,\text{bc}}$) and the flux becomes $(\mathbf{n} \cdot \mathbf{u}_\alpha) S_{\alpha,\text{bc}}$, if $\mathbf{n} \cdot \mathbf{u}_\alpha < 0$. If the velocity is also specified ($\mathbf{u}_{\alpha,\text{bc}}$), then this becomes part of the incoming flux $(\mathbf{n} \cdot \mathbf{u}_{\alpha,\text{bc}}) S_{\alpha,\text{bc}}$.

In case of specified pressure for outflow boundaries ($\mathbf{n} \cdot \mathbf{u}_\alpha > 0$), the flux is $\mathbf{n} \cdot \mathbf{u}_\alpha S_\alpha$, in which neither $\mathbf{u}_\alpha$ nor S_α are specified.

However, for inflow boundaries with specified pressure ($\mathbf{n} \cdot \mathbf{u}_\alpha < 0$), the flux is $\mathbf{n} \cdot \mathbf{u}_{\alpha,\text{bc}}S_{\alpha,\text{bc}}$, in which $\mathbf{u}_{\alpha,\text{bc}}$ is calculated using

$$\mathbf{u}_{\alpha,\text{bc}} = \underline{\underline{\sigma}}_{\alpha,\text{bc}}^{-1}\underline{\underline{\sigma}}_\alpha\mathbf{u}_\alpha, \tag{17}$$

where $\underline{\underline{\sigma}}_{\alpha,\text{bc}}$ is calculated using $S_{\alpha,\text{bc}}$.

It should be noted that this flux condition must be used in both the discretised saturation and global continuity equations, because the latter is a summation of the former. The specified pressure

condition becomes a surface flux condition in the force balance equation (Equation (4)), which effectively relaxes the pressure p to its face value counterpart p_{bc} at the boundaries.

2.7. Solving the linear equations

The global mass balance equation (Equation (10)) and force balance equations (Equation (5)) are solved by substituting $\underline{\mathbf{v}}$ and solving the system of equations for pressure. At time level $n + 1$, Equations (5) and (10) can be rewritten as

$$\begin{cases} \mathbf{M}\underline{\mathbf{v}}^{n+1} = \mathbf{C}\underline{\mathbf{p}}^{n+1} + \underline{\mathbf{s}}_u^{n+1} \\ \mathbf{B}^{\mathrm{T}}\underline{\mathbf{v}}^{n+1} = \underline{\mathbf{s}}_p^{n+1}, \end{cases}$$

respectively. Application of a discontinuous FEM for $\mathbf{v}$ leads to a block-diagonal $\mathbf{M}$ matrix that can be readily inverted, each block being local to an element. Multiplying Equation (5) by $\mathbf{B}^{\mathrm{T}}\mathbf{M}^{-1}$ and summing up with Equation (10), $\underline{\mathbf{v}}^{n+1}$ vanishes and the pressure equation is obtained

$$\mathbf{B}^{\mathrm{T}}\mathbf{M}^{-1}\mathbf{C}\underline{\mathbf{p}}^{n+1} = \underline{\mathbf{s}}_p^{n+1} - \mathbf{B}^{\mathrm{T}}\mathbf{M}^{-1}\underline{\mathbf{s}}_u^{n+1}. \tag{18}$$

Equation (18) is solved for pressure and then the velocity is obtained via Equation (5). The computationally demanding effort to solve the pressure matrix equation arising from the fully discontinuous FEM formulation is achieved using a multigrid-like approach [30]. In this case the 'fine' mesh is the one obtained by the discontinuous system, whereas the 'coarse' mesh is obtained by creating a continuous system (from the discontinuous system) by collapsing the pressure nodes. As in multigrid, the coarse mesh solution is used to accelerate the convergence of the fine mesh solution by calculating the error of the current approximation.

3. MODEL SET-UP

The numerical model is evaluated using four two-phase flow test cases (Sections 4.1–4.4). The modified Brooks–Corey model [31, 32]

$$k_{rw}\left(S_w\right) = k_{rw}^{\circ}\left(\frac{S_w - S_{wirr}}{1 - S_{wirr} - S_{nwr}}\right)^{n_w}, \tag{19}$$

$$k_{rnw}\left(S_w\right) = k_{rnw}^{\circ}\left(\frac{S_{nw} - S_{nwr}}{1 - S_{wirr} - S_{nwr}}\right)^{n_{nw}}, \tag{20}$$

where subscripts w and nw indicate wetting and non-wetting phase. k_{rw}° and k_{rnw}° are end-point relative permeability to wetting and non-weting phases, S_w and S_{nw} are the wetting and non-wetting phase volume fractions, respectively. The exponents n_w and n_{nw} are both set to 2 for all test cases.

The length of all computational domains is 1 non-dimensional length unit. Computational domain height, boundary conditions, exponents for the wetting n_w and non-wetting n_{nw} phases in the Brooks–Corey model, along with the irreducible wetting phase saturation S_{wirr}, residual non-wetting phase saturation S_{nwr} and mobility M^0 for each test case are shown in Table I.

In all test cases, the domain is initially saturated with the non-wetting phase at $(1 - S_{wirr})$. The wetting phase is then injected through the left boundary, displacing the non-wetting phase towards the opposite boundary. The wetting phase is injected at a uniform, constant velocity (u_{in}) from the left boundary for test cases 4.1 and 4.2. In test case 4.2, the inlet velocity is weighted by the

Table I. Model set-up for test cases 4.1–4.4.

	M^0	ϕ	$\mathbf{K}_1$	$\mathbf{K}_2$	$\mathbf{K}_3$	S_{wirr}	S_{nwr}	u_{in}	Δp	Height
4.1	10	0.2	1.0	N/A	N/A	0.2	0.3	0.2	N/A	N/A
4.2	10	0.4	1.0	2.5	N/A	0.1	0.2	1.0	N/A	1.0
4.3	10	0.5	1.0	10^2	N/A	0.0	0.0	N/A	1.0	0.1
4.4	4	0.2	1.0	2.0	10	0.2	0.2	N/A	1.0	0.1

Table II. Summary of the test cases performed in Section 4.

Test case	Element pairs	Dimensionality and mesh	Main features
4.1 (Buckley–Leverett)	P_1DG-P_1, P_1DG-P_2 and P_2DG-P_1DG	2D and 3D (structured/ unstructured)	Assessment of model accuracy against analytic solutions.
4.2 (Immiscible displacement)	P_1DG-P_2 and P_2DG-P_1DG	2D (coarse and fine)	Qualitative analysis of the model against lab-experiments.
4.3 (Permeability constrast and aspect ratio)	P_1DG-P_2 and P_2DG-P_1DG	2D (coarse and fine)	Numerical dispersion in high-permeability contrast.
4.4 (Channel model)	P_1DG-P_1DG and P_2DG-P_1DG	3D	Application of the method to a realistic geometry.

2D, two-dimensional; 3D, three-dimensional.
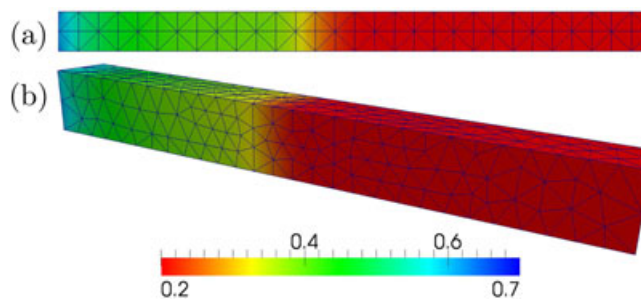
Figure 2. Wetting phase volume fraction for the Buckley–Leverett test case using the P_1DG-P_2 element pair in two-dimensional (2D) (a) and three-dimensional (3D) (b).

permeability. For test cases 4.3 and 4.4, the flow is driven by a pressure difference (Δp) between the inflow (left) and outflow (right) boundaries of the computational domain. The pressure level at the outflow boundary is set to 0 for all test cases.

For the test cases considered here, porosity ϕ is assumed uniform and, for 4.1 **K** is also uniform. However, for test cases 4.2–4.4, **K** is non-uniform and regions of constant **K** are used (subscript denotes region identities – Figures 5 and 8). For all cases, **K** is assumed isotropic.

In Section 4, four sets of numerical simulations are performed using the formulation introduced in Section 2. The main aims of these simulations (Table II) are to (i) assess numerical convergence and accuracy; (ii) validate the model against analytic (quantitative) and lab-experiments (qualitative) solutions; (iii) numerically investigate the performance of P_1DG-P_2 and P_2DG-P_1DG element pairs in multi-phase flows behaviour in highly heterogeneous media (i.e. large permeability gradient) and (iv) finally, apply it to a realistic, three-dimensional (3D), high-aspect ratio geometry.

4. RESULTS

4.1. The Buckley–Leverett test case

The Buckley–Leverett problem (non-wetting phase displaced by a wetting phase [33]) is simulated here. Despite the one-dimensional nature of the problem, 2D and 3D simulations are performed to evaluate the multi-dimensional capabilities of the model (Figure 2). The P_1DG-P_1, P_1DG-P_2 and P_2DG-P_1DG element pairs are used for these simulations.

Figures 3(a)–(c) show phase volume fraction profiles of the wetting phase for four meshes in 2D at non-dimensional time $t = 0.2$. All meshes are structured and have four elements perpendicular to the flow and 60, 120, 240 or 480 elements parallel to the flow (Figure 2(a). The geometry centre-line is used to plot these profiles. All element pairs satisfactorily capture the discontinuity in the phase volume fraction, and as the number of elements is increased, the error is reduced. Figure 3(d) shows results obtained for a Buckley–Leverett test case in 3D. A 1207-element fully unstructured mesh is used for these simulations. All the element pairs are again capable of accurately capturing the discontinuity in the phase volume fraction.
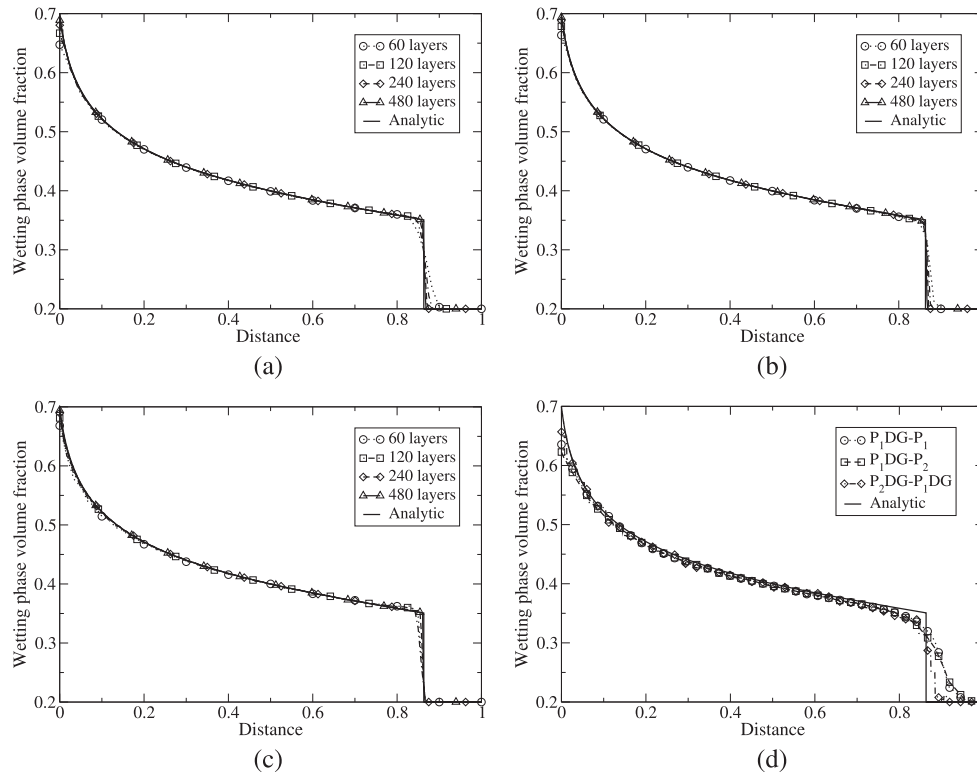
Figure 3. Wetting phase volume fraction along the geometry centre-line at non-dimensional time $t = 0.2$ for the Buckley–Leverett test case. Two-dimensional (2D) results with the P_1DG-P_1, P_1DG-P_2 and P_2DG-P_1DG element pairs are shown in (a), (b) and (c), respectively. Three-dimensional (3D) results for an unstructured mesh are shown in (d). The one-dimensional (1D) analytic solution is shown for comparison in all plots.

Figure 4(a) shows convergence rates for the results presented in Figure 3(a)–(c). The L_2 error norm of the wetting phase volume fraction is used here. Because of the discontinuity in the solution variable, a first-order convergence rate is achieved even when the high-order element pair is used (Figure 3(b)). This is because high-order methods switch to first-order upwinding at the discontinuity. Figure 4(b) shows the convergence rate of the same high-order element pair simulation (Figure 3(b)) at non-dimensional time $t = 0.3$. At this time level, the phase volume fraction field is smooth because the discontinuity has been advected out of the computational domain, and for this reason, a second-order convergence rate is achieved.

4.2. Immiscible displacement in heterogeneous porous media

This test case is designed to demonstrate the numerical robustness of the method for modelling heterogeneous porous media and it is based on the physical experiment presented by Dawe and Grattoni [34]. As shown in Figure 5, the permeability field is non-uniform.

Two sets of simulations are performed using coarse (402 elements) and fine (3714 elements) meshes; in the first set, the P_1DG-P_2 element pair is used, while in the second one, the P_2DG-P_1DG element pair is used. The time step sizes for the coarse and fine mesh simulations are 5×10^{-3} and 10^{-3} non-dimensional time units, respectively.

Figure 6 shows the wetting phase volume fraction maps at time $t = 0.16$ for all four simulations. Results for the P_1DG-P_2 element pair set of simulations is shown in the top row. Results for the P_2DG-P_1DG element pair set of simulations is shown in the bottom row.

A physical experiment with similar set-up was performed by Dawe and Grattoni [34] to investigate miscible and immiscible displacement in heterogeneous permeability and wettability cases. For immiscible displacement, the wetting phase was uniformly injected at rate of $\approx$ 1ml/min in a
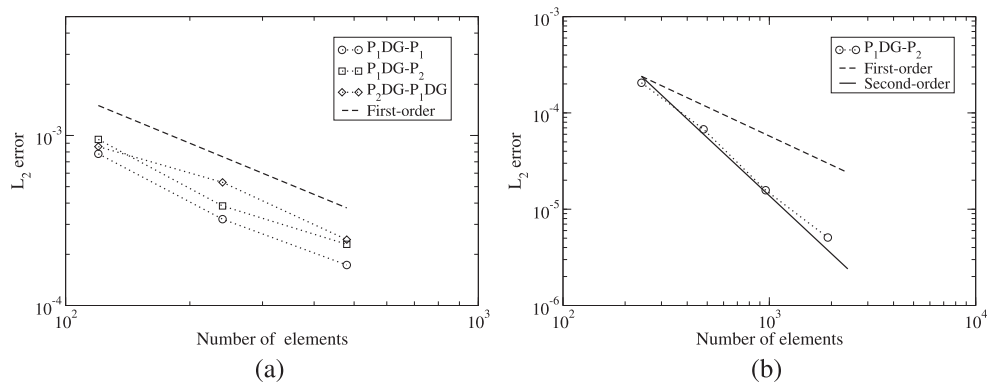
Figure 4. Error metrics versus number of elements for the Buckley–Leverett test case for element pairs P$_1$DG-P$_1$, P$_1$DG-P$_2$ and P$_2$DG-P$_1$DG in two-dimensional (2D).
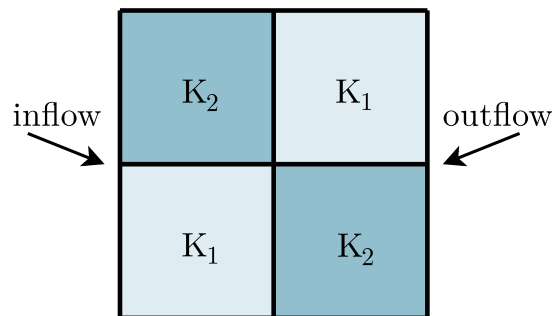

Figure 5. Schematic of the computational domain along with the material properties and boundary conditions for the heterogeneous permeability test case. Darker areas ($\mathbf{K}_1$) represent regions with high permeability.
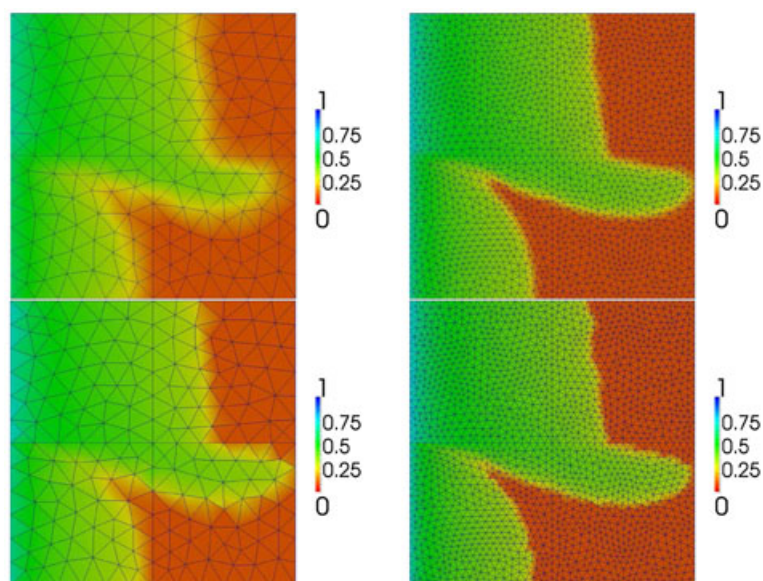

Figure 6. Wetting phase volume fraction maps at time $t = 0.16$ for the heterogeneous permeability test case. Top row: P$_1$DG-P$_2$ elements. Bottom row: P$_2$DG-P$_1$DG elements. Left column: coarse mesh. Right column: fine mesh. The meshes used for these simulations are also shown here.
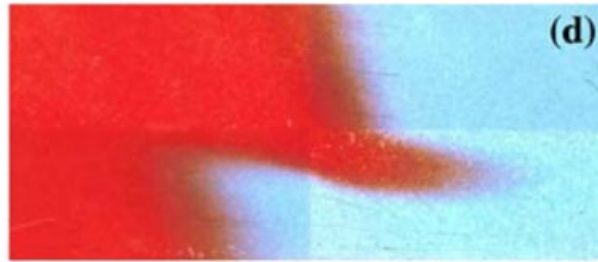
Figure 7. Wetting phase volume fraction map obtained from the experiment performed by Dawe and Grattoni (extracted from [34]). Red contour indicates the injected fluid breakthrough. Geometry and permeability distribution used in this experiment is the same as shown in Figure 5.
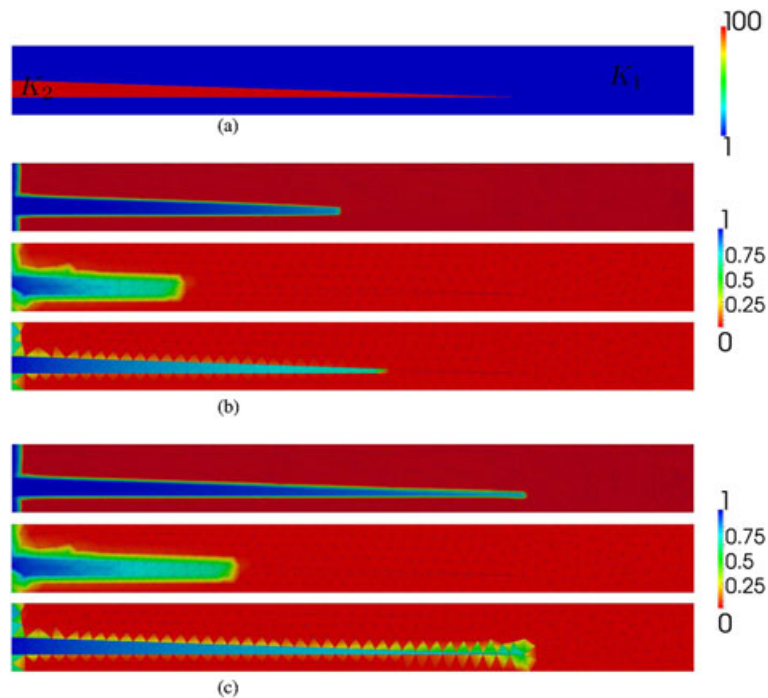

Figure 8. Schematic of the computational domain along with the permeability map for the high-permeability wedge-shaped region test case (a). Snapshots of the wetting phase volume fraction field for a fine mesh P_1DG-P_2 simulation (top), coarse mesh P_1DG-P_2 simulation (middle) and coarse mesh P_2DG-P_1DG simulation (bottom) at non-dimensional times $t = 0.011$ (b) and $t = 0.0014$ (c). The meshes used for these simulations are also shown in (b) and (c).

domain of 20 cm×10 cm×0.6 cm. Glass ballotini beads produced porosity of 0.4. The permeability ratio was 2.5.

Snapshots in Figure 6 show the wetting phase flood 'fingering' across the four region intersection, demonstrating the preferential flow through high-permeability regions. This is in good qualitative agreement with the experimental results (Figure 7, taken from Dawe and Grattoni [34]).

4.3. High-permeability high-aspect ratio region

Fractures and cracks in porous media are ubiquitous; however, they are not easy to model because of their high-aspect ratio and small size compared with the reservoir domain. Nonetheless, cracks may have a dramatic impact in the overall behaviour of the flow as they can channelise the flow through them. Usually, they are characterised by a thin tip and a high permeability. A simplified 2D wedge-shaped high-permeability region embedded in a rectangular low-permeability domain is considered here. The permeability map is shown in Figure 8. The wedge aspect ratio is $1/30$, and its maximum height is 0.025.
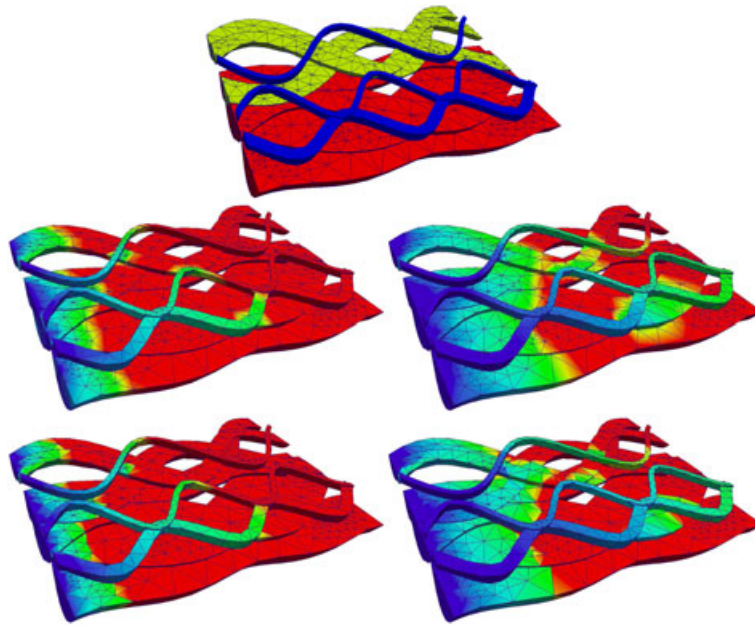
Figure 9. Schematic of the computational domain along with the permeability map and mesh used for the three-dimensional (3D) fluvial channel case (top). The most permeable channels (K_3) are shown in blue, the least permeable channels (K_1) are shown in red and channels with permeability K_2 are shown in green. Wetting phase volume fraction maps at two time levels (left and right). P_1DG-P_1 element pair results are shown in the middle row. P_2DG-P_1DG element pair results are shown in the bottom row.

Three numerical simulations are performed in total. Two use the P_1DG-P_2 element pair, and one uses the P_2DG-P_1DG element pair. P_1DG-P_2 element pair simulations are performed using a coarse (672 elements) and a fine (56 902 elements) mesh. The coarse mesh is used for the P_2DG-P_1DG element pair simulation.

Figure 8 shows wetting phase volume fraction maps at non-dimensional times $t = 0.011$ and 0.014. The P_1DG-P_2-based solutions disperse the wetting phase into the low-permeability matrix. This is more pronounced for the coarse mesh simulation. It can be seen how the front of the wetting phase is considerably delayed compared with the other two simulations. On the other hand, the P_2DG-P_1DG solution does not disperse the wetting phase into the matrix and even a very coarse mesh is sufficient to accurately capture the flow.

4.4. Three-dimensional fluvial channel model

The method is finally applied to a subsurface example of high-permeability fluvial sandstone channels embedded in a low permeability mudstone background. Such features are often observed in aquifers and petroleum reservoirs. Because of the importance of these channels to the flow behaviour, their correct representation and resolution is key to obtain reliable productivity solutions. An extensive review on how challenging this is for conventional simulators can be found in [27] and is not discussed here. This problem is chosen precisely because it cannot be easily solved using traditional methods. In this model, three different sets of highly permeable channels are considered. The mesh and permeability map for these simulations are shown in Figure 9 (top). The thin channels have a permeability of K_3, the medium size channels K_2 and the wide channels K_1. It is worth noting that $K_3 = 5K_2 = 10K_1$ (Table I).

Two numerical simulations are performed using an 8000-element fully unstructured mesh. Wetting phase volume fraction maps at two time levels are shown in Figure 9. Results for the P_1DG-P_1DG element pair are shown in the middle, while results for the P_2DG-P_1DG element pair are shown in the bottom row. Results are in reasonable agreement. It is worth noting that the P_1DG-P_1 element pair (closest to traditional CVFEM formulation) is numerically more dispersive

(see Section 4.3 or [28]). Nevertheless, these results demonstrate the potential of the methods presented here to simulate real-world geometries.

5. CONCLUSIONS

A novel CVFEM formulation based on P_nDG-P_m(DG) element pairs with nth-order representation for velocity and mth-order for pressure has been presented. The main advantages of this formulation over existing ones is that arbitrarily high-order polynomial representation for pressure and velocity can be used and it is high-order accurate in space and time. In P_nDG$-P_{n+1}$ element pairs, velocity is discontinuously defined by polynomials of order n whereas pressure is continuously represented by polynomials of order $n+1$ with CVs spanning various neighbours elements, as exemplified by Figure 1(a). However, in the novel P_{n+1}DG-P_nDG element pair, introduced in this paper, both pressure and velocity have discontinuous representation with polynomials of order n and $n+1$, respectively. In this family of element pairs, CVs do not span elements (Figure 1(b), which resolves a long-standing problem associated with the use of traditional CVFEM formulations in heterogeneous porous media flows.

The new formulation was evaluated using the Buckley–Leverett benchmark and first-order convergence rates were achieved for solutions with discontinuities, which are not common in the literature [35, 36]. Second-order convergence rates were achieved for solutions without a discontinuity. More numerical simulations were performed to demonstrate the capabilities of the methods presented under heterogeneous and high-aspect ratio computational domains. It was shown that the method is able to successfully resolve multi-phase flows under those circumstances. Furthermore, the P_{n+1}DG-P_nDG element pair was shown to completely remove numerical dispersion induced by heterogeneous permeabilities.

The formulation presented here was implemented in the open-source software framework Fluidity for multi-phase flows (IC-Ferst) and it has been extended to include/model multi-component/interface-capturing flows [29, 37, 38], segregation in granular flows [39] and oil reservoir flows [27, 40, 41].

REFERENCES

1. Chen Z, Huan G, Ma Y. *Computational Methods for Multiphase Flows in Porous Media*. SIAM, 2006.
2. AIEA. Use of natural analogues to support radionuclide transport models for deep geological repositories for long-lived radioactive wastes, AIEA, 1999.
3. Pruess K. Numerical modeling of gas migration at a proposed repository for low and intermediate level nuclear wastes. *Technical Report Report LBL-25413*, Lawrence Berkeley Laboratory: Berkeley, USA, 1990.
4. Jiang X. A review of physical modelling and numerical simulation of long-term geological storage of carbon dioxide. *Applied Energy* 2011; **88**:3557–3566.
5. Aziz K, Settari A. *Fundamentals of Reservoir Simulation*. Elsevier Applied Science Publishers: New York, 1986.
6. Chen Z, Ewing RE. Comparison of various formulations of three-phase flow in porous media. *Journal of Computational Physics* 1997; **132**(2):362–373.
7. Chen Z, Huan G, Wang H. Simulation of a compositional model for multiphase flow in porous media. *Numerical Methods for Partial Differential Equations* 2005; **21**(4):726–741.
8. Chavent G, Jaffré J. *Mathematical Models and Finite Elements for Reservoir Simulation, Studies in Mathematics and Its Applications*, Vol. 17. Elsevier: Amsterdam, 1986.
9. Forsyth P. A control volume, finite element method for local mesh refinement in thermal reservoir simulation. *SPE Resevoir Engineering* 1990; **5**(4):561–566.

10. Cordazzo J, Maliska C, da Silva A, Hurtado F. The negative transmissibility issue when using CVFEM in petroleum reservoir simulation – 1. Theory. In *Proceedings of the 10th Brazilian Congress of Thermal Sciences and Engineering – ENCIT 2004*. Brazilian Society of Mechanical Engineering – ABCM: Rio de Janeiro, Brazil, 2004.

11. Geiger S, Roberts S, Matthäi S, Zoppou C, A Burri A. Combining finite element and finite volume methods for efficient multiphase flow simulations in highly heterogeneous and structurally complex geologic media. *Geofluids* 2004; **4**(4):284–299.

12. Hurtado F, Maliska C, Silva AFC, Cordazzo J. A quadrilateral finite element-based finite-volume formulation for the simulation of complex reservoirs. *SPE* 2007; **107444**.

13. Huber H, Helmig R. Node-centered finite volume discretizations for the numerical simulation of multiphase flow in heterogeneous porous media. *Computers & Geosciences* 2000; **4**:141–164.

14. Helmig R. *Multiphase Flow and Transport Processes in the Subsurface*. Springer-Verlag: Berlin, 1997.

15. Durlofsky LJ. A triangle-based mixed finite element finite volume technique for modelling two-phase flow through porous media. *Journal Computational Physics* 1993; **105**:252–266.

16. Durlofsky LJ. Accuracy of mixed and control volume finite element approximations to Darcy velocity and related quantities. *Water Resources Research* 1994; **30**:965–973.

17. Cumming B, Moroney T, Turner I. A mass-conservative control volume-finite element method for solving Richards' equation in heterogeneous porous media. *BIT Numerical Mathematics* 2011; **51**(4):845–864.

18. Kirkland M, Hills R, Wierenga P. Algorithms for solving Richards' equation for variably saturated soils. *Water Resources Research* 1992; **28**:2049–2058.

19. Cumming B. Modelling sea water intrusion in coastal aquifers using heterogeneous computing. *PhD Thesis*, Queensland University of Technology, Australia, 2012.

20. Nick H, Matthai S. Comparison of three FE–FV numerical schemes for single- and two-phase flow simulation of fractured porous media. *Transport in Porous Media* 2011; **90**:421–444.

21. Nick H, Matthai S. A hybrid finite element–finite volume method with embedded discontinuities for solute transport in heterogeneous media. *Vadose Zone Journal* 2011; **10**:299–312.

22. Brooks A, Hughes T. Streamline upwind Petrov–Galerkin formulations for convection dominated flows with particular emphasis on the incompressible Navier–Stokes equations. *Computer Methods in Applied Mechanics and Engineering* 1982; **32**:199–259.

23. Tezduyar T, Park Y. Discontinuity-capturing finite element formulations for nonlinear convection–diffusion–reaction equations. *Computer Methods in Applied Mechanics and Engineering* 1986; **59**:307–325.

24. Rivière B, Wheeler M, Banas K. Part 2: Discontinuous Galerkin method applied to a single-phase flow in porous media. *Computers & Geosciences* 2000; **4**:337–349.

25. Rivière B, Wheeler M. Discontinuous Galerkin methods for flow and transport problems in porous media. *Communications in Numerical Methods in Engineering* 2002; **18**:63–68.

26. Bastian P. Higher order discontinuous Galerkin methods for flow and transport in porous media. In *Challenges in Scientific Computing - CISC 2002*, Bansh E (ed।)., Lecture Notes in Computational Science and Engineering. Springer: Berlin, Germany, 2002.

27. Jackson M, Gomes J, Mostaghimi P, Percival J, Tollit B, Pavlidis D, Pain C, AH El-Sheikh SP, Muggeridge A, Blunt M. Reservoir modeling for flow simulation by use of surfaces, adaptive unstructured meshes, and an overlapping-control-volume finite-element method. *SPEREE* 2015. DOI: http://dx.doi.org/10.2118/163633-PA.

28. Su K, Latham JP, Pavlidis D, Xiang J, Fang F, Mostaghimi P, Percival JR, Pain CC, Jackson MD. Multiphase flow simulation through porous media with explicitly resolved fractures. *Geofluids* 2016; **15**:592–607.

29. Pavlidis D, Gomes J, Xie Z, Percival J, Pain C, Matar O. Compressive-advection and multi-component methods for interface-capturing. *International Journal for Numerical Methods in Fluids* 2015; **80**:256–282.

30. Brandt A. Multilevel adaptive solutions to boundary-value problems. *Mathematics of Computation* 1977; **31**: 333–390.

31. Alpak F, Lake L, Embid S. Validation of a modified Carman-Kozeny equation to model two-phase relative permeabilities. In *1999 SPE Annual Technical Conference and Exhibition*. SPE: Houston, Texas, 1999. SPE 56479.

32. Brooks R, Corey A. Hydraulic properties of porous media. In *Hydrology Papers*, Vol. 3, Colorado State University, 1964.

33. Buckley S, Leverett M. Mechanism of fluid displacements in sands. *Transactions of the American Institute of Mining, Metallurgical, and Petroleum Engineers* 1942; **146**:107–116.

34. Dawe RA, Grattoni CA. Experimental displacement patterns in a 2×2 quadrant block with permeability and wettability heterogeneities problems for numerical modelling. *Transport in Porous Media* 2008; **71**:5–22.

35. Schmid K, Geiger S, Sorbie K. Higher order FE–FV method on unstructured grids for transport and two-phase flow with variable viscosity in heterogeneous porous media. *Journal of Computational Physics* 2013; **241**(0):416–444.

36. Hoteit H, Firoozabadi A. Numerical modeling of two-phase flow in heterogeneous permeable media with different capillarity pressures. *Advances in Water Resources* 2008; **31**(1):56–73.

37. Pavlidis D, Xie Z, Percival J, Gomes J, Pain C, Matar O. Two- and three-phase horizontal slug flow modelling using an interface-capturing compositional approach. *International Journal for Multiphase Flow* 2014; **67**:85–91.

38. Xie Z, Pavlidis D, Percival J, Gomes J, Pain C, Matar O. Adaptive unstructured mesh modelling of multiphase flows. *International Journal for Multiphase Flow* 2014; **67**:104–110.

39. Percival J, Pavlidis D, Xie Z, Gomes J, Matar O, Sakai M, Takahashi H, Pain C. Transport and segregation of sand and granular flows in fluidized beds. *International Journal for Multiphase Flow* 2014; **67**:191–199.

40. Mostaghimi P, Percival J, Pavlidis D, Ferrier R, Gomes J, Gorman G, Jackson M, Neethling S, Pain C. Anisotropic mesh adaptivity and control volume finite element methods for numerical simulation of multiphase flow in porous media. *Mathematical Geoscience* 2015; **347**:673–676.

41. Salinas P, Percival JR, Pavlidis D, Xie Z, Gomes J, Pain CC, Jackson MD. A discontinuous overlapping control volume finite element method for multi-phase porous media flow using dynamic unstructured mesh optimization. *SPE 173279*, Houston, Texas, 2015. DOI: http://dx.doi.org/10.2118/173279-MS.